Hole doping and electronic correlations in Cr substituted BaFe$_2$As$_2$

M. R. Cantarino[1,2,*], K. R. Pakuszewski[3], B. Salzmann[4], P. H. A. Moya[1], W. R. da Silva Neto[1], G. S. Freitas[3], P. G. Pagliuso[3], C. Adriano[3], W. H. Brito[5], F. A. Garcia[1,6,*]

1 Instituto de Física, Universidade de São Paulo, 05508-090 São Paulo, SP, Brazil
2 European Synchrotron Radiation Facility, BP 220, F-38043 Grenoble Cedex, France
3 Instituto de Física "Gleb Wataghin", UNICAMP, 13083-859, Campinas-SP, Brazil
4 Département de Physique and Fribourg Center for Nanomaterials, Université de Fribourg, CH-1700 Fribourg, Switzerland
5 Departamento de Física, Universidade Federal de Minas Gerais, C.P. 702, 30123-970, Belo Horizonte, MG, Brazil
6 Ames Laboratory, U.S. DOE, and Department of Physics and Astronomy, Iowa State University, Ames, Iowa 50011, USA
* Corresponding authors M.R.C. (marli.cantarino@esrf.fr) and F.A.G. (fgarcia@if.usp.br)

Abstract

The absence of superconductivity (SC) in Cr-substituted BaFe$_2$As$_2$ (CrBFA) is a well-established but poorly understood topic. It is also established that the suppression of the spin density wave transition temperature (T_{SDW}) in CrBFA and Mn-substituted BaFe$_2$As$_2$ (MnBFA) almost coincides as a function of the Cr/Mn concentrations, irrespective of the putative distinct electronic effects of these substitutions. In this work, we employ angle-resolved photoemission spectroscopy (ARPES) and combined density functional theory plus dynamical mean field theory calculations (DFT+DMFT) to address the evolution of the Fermi surface (FS) and electronic correlations in CrBFA. Our findings reveal that incorporating Cr leads to an effective hole doping of the states near the FS in a way that can be well described within the virtual crystal approximation (VCA). Moreover, our results show orbital-specific correlation effects that support the Hund localization scenario for the CrBFA phase diagram. We found a fractional scaling of the imaginary part of self-energy as a function of the binding energy, which is a signature property of Hund's metals. We conclude that CrBFA is a correlated electron system for which the changes in the FS as a function of Cr are not related to the suppression of T_{SDW}. Rather, this suppression and the absence of SC are primarily due to the competition between Cr local moments and the Fe-derived itinerant spin fluctuations.

1   Introduction

The discovery of superconductivity (SC) in hole-doped $LaO_{1-x}F_xFeAs$ [1] led to the new field of the iron-based superconductors (FeSCs). A superconducting critical temperature (T_{SC}) as high as ≈ 55 K in hole-doped $SmO_{1-x}F_xFeAs$ was soon after reported [2] and remains to date among the highest so far observed in this diverse family of materials [3].

The $BaFe_2As_2$ (BFA) material is a particularly well-explored parent compound of the FeSCs. It undergoes an antiferromagnetic (spin density wave, SDW) transition with a critical temperature (T_{SDW}) of ≈ 133.7 K that is preempted by an almost concomitant tetragonal to orthorhombic phase transition [4, 5]. In BFA, partial chemical substitutions on the Ba, Fe or As sites can stabilize high-temperature superconductivity (HTSC) [6, 7, 8, 9, 10, 11]. The highest T_{SC}, ≈ 38 K, is observed when Ba is partially substituted by an Alkaline metal, as in $Ba_{1-x}\ A_xFe_2As_2$ (A = K or Cs) [12, 13], corresponding to nominal hole doping.

In all cases wherein HTSC emerges in BFA substituted phases, the composition (x) *vs.* temperature (T) phase diagram shows that the maximum T_{SC} is observed in a x range wherein the T_{SDW} is fully suppressed. This phenomenology suggested a close link between fluctuations of the magnetically ordered phase and the formation of HTSC, which is part of the consensus in this research field [14]. The relevant energy scales to understand the FeSCs, however, remain under debate.

Low energy effective models contain some essential ingredients to understand the phase diagrams of many FeSCs [15, 16]. This scenario posits that the SDW phase is the result of a nested Fermi surface (FS) and that charge doping detunes the nesting condition, thus suppressing T_{SDW}. The resulting fluctuations boost the SC pairing. Other descriptions adopt the Fe^{2+} $3d^6$ local electronic structure as a starting point. The resulting large spins are lowered by kinetic frustration and the main energy scales are provided by the on-site electron-electron Hund's exchange and by the Coulomb interactions [17, 18, 19, 20]. Within the latter framework, the FeSCs are classified as Hund's metals, a new class of strongly correlated materials, where the strength of correlations are sensitive to the Fe-$3d$ occupancy, Hund's coupling J_H, and to the pnictogen/chalcogen height. More importantly, the Hund's metals exhibit an orbital(charge) and spin separation for a broad intermediate temperature region, where the orbital(charge) are itinerant and the spin degrees of freedom are quasi-localized [21]. The resulting HTSC phase from this electronic correlated state displays an universal heat capacity associated with $2\Delta_{max}/T_{SC} = 7.2 \pm 1$ (where Δ_{max} is the maximum SC gap) which can be explained by taking into account the incoherent nature of local spin fluctuations [22].

To distinguish between possible scenarios, it is key to probe how chemical substitutions change the electronic structure of the FeSCs. In this context, an intriguing asymmetry is observed in the phase diagram of transition metal substituted BFA: SC is not observed in the Cr [23], Mn [24] or V [25] substituted materials, which corresponds to the nominal hole doping. Particular attention has been devoted to the Mn and, to a lesser degree, Cr substituted materials (hereafter called, respectively, MnBFA and CrBFA).

In the case of MnBFA, the absence of SC was first ascribed to the lack of charge doping by Mn [26, 27]. A complete scenario, however, encompasses the scattering of the Fe-derived

excitations promoted by the Mn-derived excitations [28, 29], a weak charge doping effect caused by Mn, electronic disorder and correlations [30], which is in line with theoretical calculations [31, 32, 33].

It was soon noted that the CrBFA and MnBFA x vs. T phase diagrams look very similar, with the suppression of T_{SDW} depending only on x [24]. Indeed, both Cr and Mn induce a crossover from an itinerant to a more localized form of magnetism [34, 35] and, as in MnBFA, it is suggested that the Fe-SDW and Cr-Néel fluctuations compete for the ground state [23, 36, 37, 38]. Similar effects are caused by Cr-substitutions in Ni-doped BFA [39, 40, 41] as well as in P-substituted BFA [42]. Disordered magnetism, however, is only observed in MnBFA [43]. In addition, the role of Cr as a hole dopant is observed in Ni-doped BFA [39] but recent angle-resolved photoemission spectroscopy (ARPES) experiments of Cr-substituted $CsFe_2As_2$ do not support hole doping caused by Cr [44]. All this phenomenology suggests that, as in the MnBFA phase diagram, the Cr effects on the electronic structure and correlations in CrBFA require clarification.

This work is dedicated to understanding hole doping and electronic correlations in CrBFA. We employed ARPES experiments and density function theory in combination with dynamical mean-field theory (DFT+DMFT) calculations of the excitation spectra of $Ba(Fe_{1-x}Cr_x)_2As_2$ ($x = 0.0$, 0.03 and 0.085, hereafter called the BFA, Cr3% and Cr8.5% materials, respectively). Our results show that Cr is an effective hole dopant, as in the case of K substitution [45], with the DFT+DMFT calculations capturing the experimentally observed changes in size and shape of the hole and electron pockets. Hence, the suppression of T_{SDW} in CrBFA is similar to that of MnBFA, irrespective of the action of Cr as a hole dopant.

Moreover, based upon the experimental ARPES spectral function, we analyze electronic correlations in CrBFA and show that the imaginary part of the self-energy, $Im\Sigma(E_B)$ presents a Cr-dependent fractional scaling as a function of the binding energy (E_B), the hallmark of a Hund's metal [46]. These features are also well reproduced by our calculations, including the Cr dependency on the fractional exponent. Thus, it is suggested that Cr tunes the BFA electronic structure into the non-Fermi liquid "spin-freezing" regime [47].

2   Materials and methods

Single crystals of $Ba(Fe_{1-x}Cr_x)_2As_2$ were synthesized by an In-flux method [48]. The resulting crystals were crushed and sieved into a fine powder for X-ray diffraction (XRD) experiments to check the crystallographic phase and determine lattice parameters. The final Cr content was checked by energy-dispersive x-ray spectroscopy (EDS) measurements. Physical properties (resistivity and specific heat) were characterized by a commercial Physical Properties Measurement System (PPMS) from Quantum Design. Results from EDS and physical properties were compared to composition vs. T phase diagrams in literature [23, 35, 36] to benchmark the values of x.

The samples with $x = 0.0$, $x = 0.03$, and $x = 0.085$ were selected for ARPES measurements at the Bloch beamline of the Max IV synchrotron in Lund, Sweden. The ARPES spectra were obtained using the Scienta DA30 photoelectron analyzer for incident photon energies between 60 and 81 eV. At this photon energy, an energy resolution of about 8 to 10 meV and angular resolution of 0.1° was achieved. The samples were glued on a Mo sample holder using silver epoxy. An Al post was glued at the top of each sample for subsequent cleaving. The post was removed inside the main preparation chamber (vacuum of 3×10^{-10} mbar). The samples were then transferred to the analyzer chamber, at 2×10^{-11}
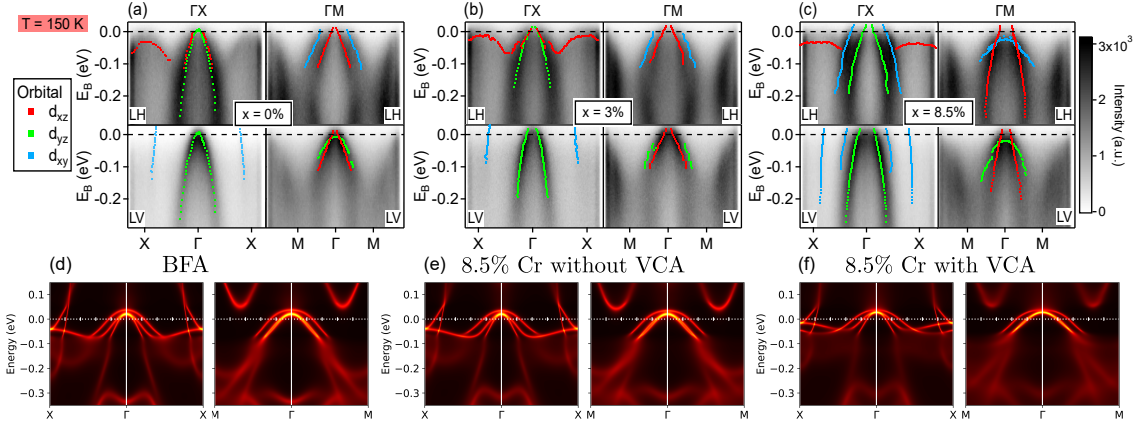
Figure 1: (*a*)-(*c*) Overview of the ARPES measured electronic band structure of the BFA, Cr3% and Cr8.5% materials. As indicated, measurements were taken along the ΓX and ΓM directions and for LH and LV polarizations. The dots represent the band positions as obtained from the second derivative of the band maps and MDC analysis. (*d*)-(*f*) DFT+DMFT obtained spectral functions for the paramagnetic phases at T = 150 K for (*d*) BFA, (*e*) the Cr8.5% material only with the structural change (no VCA), and (*f*) and Cr8.5% in the VCA approximation.

mbar.

The Brillouin zone (BZ) high-symmetry directions are labeled according to the crystal body-centered tetragonal structure. The results presented were measured at the samples' tetragonal PM state (T = 150 K). During experiments, we probe the high-symmetry directions ΓX and ΓM for both Γ and Z k_z levels. We employed linear horizontal (LH) and vertical (LV) polarization to probe different Fe-3d orbital contributions to the ARPES intensity.

The DFT+DMFT calculations were performed using the fully charge self-consistent DFT + embedded-DMFT approximation [49] at 150 K. The DFT calculations were performed within the full potential linearized augmented plane wave method and Perdew-Burke-Ernzehof generalized gradient approximation (PBE-GGA) [50], as implemented in WIEN2k package [51]. The DMFT impurity problem was solved by using continuous-time quantum Monte Carlo (CTQMC) calculations [52], and rotationally invariant interaction with U = 5.0 eV and Hund's coupling J = 0.8 eV. Similar U and J values were successfully employed in Ref. [18] within the same implementation.

To calculate the spectral functions and Fermi surfaces we performed the analytical continuation of the calculated self-energies using the maximum entropy method [49]. For the double-counting correction term, we used the standard fully localized-limit form [53] with nominal occupancy n_d^0 = 6. We used the experimental crystal structures obtained by XRD and the Cr doping was simulated within the virtual crystal approximation (VCA).

3   Results and discussion

An overview of the experimentally determined electronic band structures of CrBFA is presented in Fig. 1(*a*)-(*c*). The experimental geometries, beam polarization (either LH or LV polarizations), and the sample's Cr content are indicated in each panel. For all samples and measurement conditions, the band features are well observed allowing their

characterization as a function of Cr.

The band positions are marked by the colored dots determined from the second derivatives of the band maps and from Momentum and Energy Distribution Curves (MDCs and EDCs, respectively). Indeed, having the spectral function a Lorentzian lineshape, its central position is the minimum of the second derivatives. This method, therefore, describes the band shape and effective mass to a point but ignores information about the one-particle excitation lifetime and scattering rate.

For this family of materials, the electronic bands derived from the Fe $3d$-states are subjected to the As ligand effects. This effect breaks the Fe $3d$-states degeneracy and imparts a strong orbital character to the electronic bands in the FeSCs [3, 14]. The distinct orbital characters are labeled by dots of distinct colors and were determined by the selection rules for the ARPES intensity polarization dependence and guided by previous works [54, 55, 56, 57].

The Cr hole doping effect on the bands forming the hole pockets around Γ is visible from direct inspection of the data. Indeed, the hole pocket Fermi vectors, k_F, are increasing with Cr introduction, in line with the expectation of hole-doping by Cr substitution. A change in the polarization selection rules with Cr substitution is also observed in the case of the 8.5%Cr, where the spectral weight of the outer hole pocket is seen in the region expected for bands with $d_{xz/yz}$ main orbital character, for measurements along the ΓX direction. This is evidence that the main orbital character of the d_{xy} derived bands and their hybridization is significantly affected by Cr, as observed for Co substitution [58].

The change in hybridization may result from the structural changes caused by Cr substitutions. It may affect the bands even if charge doping is weak, as concluded from experiments of MnBFA samples [30, 59]. To tell apart the structural and charge doping effects, we calculate the spectral functions of pristine BFA (Fig. 1(d)) and of Cr8.5% doped BFA (Figs. 1(e)-(f)) within our DFT+DMFT approximation. In particular, we adopted two strategies to capture the effects caused by Cr, namely: i) first, the calculations were performed using only the Cr8.5% crystal structure to take into account the effects of the new electronic hybridization; and then ii) the calculations were performed freezing the structure as that of BFA, but considering charge doping effects within the virtual crystal approximation (VCA).

By direct inspection, the change in k_{F}, and therefore in the sizes of the hole pockets, is well reproduced by the VCA approximation alone, evidencing the role of Cr as a hole dopant. Therefore, whereas changing hybridization is an integral part of the CrBFA electronic structure, as discussed in the case of the d_{xy} derived bands, charge doping dominates the change in the size of the hole pockets closer to the Fermi level in CrBFA. From now on, we will focus on DFT+DMFT results within the VCA approximation, emphasizing that it does not account for all experimentally observed effects.

It is intriguing to observe that both in the experiment and theoretical calculations, the corresponding change in the size of electron pockets due to doping is not readily observed along the ΓX direction. We thus inspect in Figs. 2(a)-(c) the experimentally obtained FSs, for the three samples. The data suggest that the electron pockets are changing, evolving from an idealized elliptical shape in BFA to a more petal-like shape in CrBFA. It also suggests that the pockets are shrinking in a direction other than the $\Gamma X(Y)$ direction. To guide our analysis, we present in Figs. 2(e)-(f) the corresponding DFT+DMFT calculations of the three-dimensional FSs of our materials, along with cuts of the Γ-centered FSs. These FSs were obtained by considering vanishing scattering rates at the chemical potential.

The calculations show all three hole pockets increasing upon Cr introduction, but the decrease of the electron pockets area is not as clear. The calculated electron pockets for
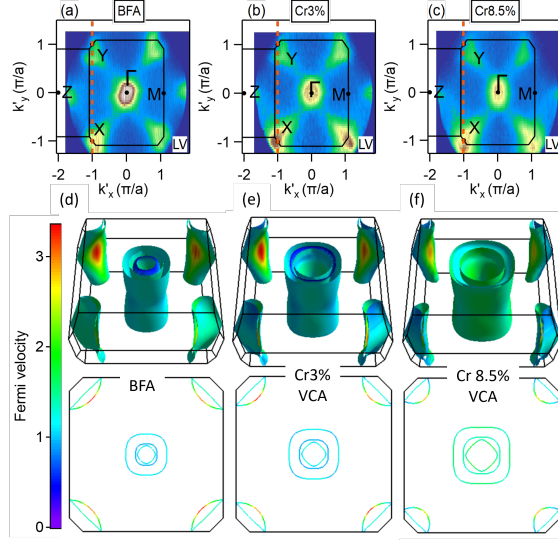
Figure 2: $(a) - (c)$ Measured Fermi Surface of the BFA, Cr3% and Cr8.5% materials with LV polarization, showing the BZ draw and its high-symmetry points. The red dashed line indicates the XY cut based upon which the electron pockets of $3(h)$ were reconstructed. $(d)-(f)$ DFT+DMFT paramagnetic $(T = 150$ K) Fermi Surface for BFA, Cr3% and Cr8.5%. The Cr substituted results were calculated using VCA.

the doped samples show a protuberant shape along the ΓX direction and seem to decrease along the XY direction. This motivates the exploration of different high-symmetry cuts of the experimentally obtained electron pocket bands as a function of Cr content. From the ARPES band map measurements, it is possible to extract the electronic band as a function of $k_{y(x)}$ and E_B for other high-symmetry directions by fixing the map $k_{x(y)}$ to a high-symmetry point and reconstructing the energy bands.

The YZ and XY cuts can be adopted to capture the changes in electron pockets as a function of Cr. These cuts are represented as green and magenta dashed lines #1 and #2 in Figs. $3(a)$-(b) for the Cr8.5% sample. The red dashed lines in Figs. $2(a)$-(c) represent the XY cut for all three samples. The full set of electronic band positions as a function of Cr content is compiled in Figs. $3(c)$-(h), of which (f) and (h) present band positions extracted from the mentioned YZ and XY cuts, respectively. The measurement conditions and main orbital characters attributed to each band are labeled on each figure, where the darker points represent the parent compound and lighter points represent a larger Cr content. The electron pocket along the YZ direction has different selection rules since it is related to the inner section of the electron pocket, also interpreted as the minor axis of an idealized ellipse.

More specifically, in Figs. $3(c)$-(e), the Cr-dependent evolution of the hole pockets is presented. The tendency of increasing hole pockets is clear for all bands as is indeed observable by direct inspection of the band measurements (Fig. 1). Figs. $3(f)$-(h) present the electron pockets evolution. The measurements along ΓX in Fig. $3(g)$ show a weak Cr-dependency. In the case of Figs. $3(f)$ and (h), the reconstructed bands from the Fermi maps have lower resolution, due to the electron analyzer collection mode, and even with second derivative analysis the data are not as well-defined as those obtained from the band maps. This is illustrated in the two panels of Fig. $3(i)$, wherein representative second derivative data of this band reconstruction is presented.

To better visualize the band evolution, we can study the Fermi vectors k_F as a function
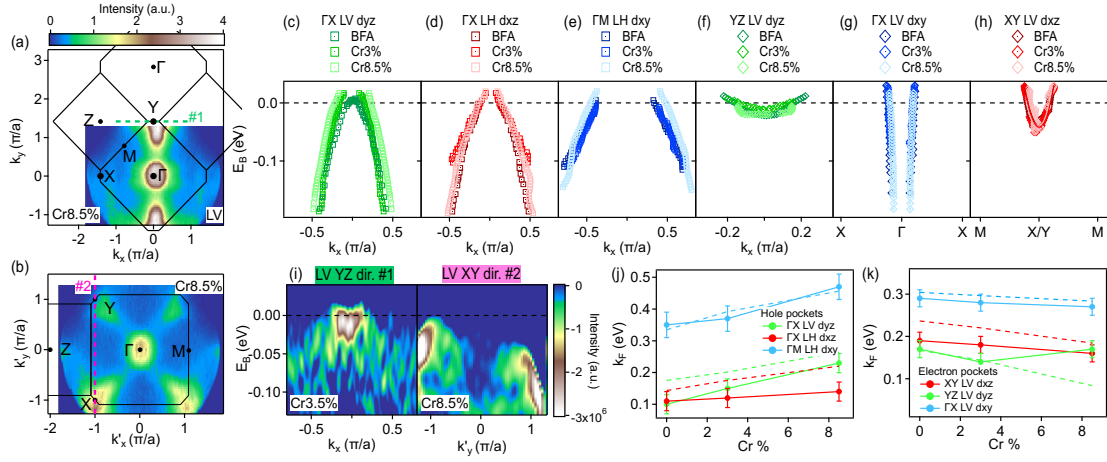
Figure 3: (a) and (b) experimentally determined FSs of the Cr8.5% sample. Measurements were performed adopting LV polarization at two different geometries. The BZ and high-symmetry points are indicated for reference and the colored dashed lines (green and magenta) are guides to eyes indicating the FS cuts #1 and #2 from which we extract the data to reconstruct the electron pockets presented in (f) and (h). (c) − (f) Survey of the band state positions, in the vicinity of E_F, obtained from the fitting of the second derivatives of the MDCs for different Cr content. In each panel, experimental conditions are indicated. (i) YZ and XY second derivative energy maps reconstructed from cut #1 and #2 for the Cr3.5% and Cr8.5% samples respectively. (j) and (k) Evolution of Fermi vectors (k_F) as a function of Cr content for hole pockets and electron pockets. The dashed lines represent the k_F values predicted by our calculations.

of Cr content and compare the results with the theoretically calculated values. The Fermi vectors are the momentum points where a certain band crosses the Fermi level, characterizing the pocket sizes and their respective increasing/decreasing associated with effective charge doping. In Fig. 3(j), the filled circles show the experimental k_F values of the hole bands, and the dashed lines represent the theoretical results, extracted from the Fermi surfaces of Figs. 2(d)-(f). The experimental data seems to follow the predicted trend, with excellent agreement observed in the case of the outer hole pocket of d_{xy} main character. Due to the multiband nature of the electronic structure, it is hard to disentangle the contributions of the inner and middle hole pockets of $d_{xz/yz}$ main orbital character, and the agreement is not as good. Nevertheless, the trend stands and we can affirm that the VCA calculation correctly describes the effective hole doping and hole pocket increasing.

As for the electron pockets, the predicted decrease in the electron pocket size is small, and experimentally, the variation of k_F could be considered constant within error bars, as shown in 3(k). For the electron pocket extracted from the high-statistic electron bands along the ΓX direction (d_{xy} orbital character), one can observe that the experimental data is in excellent agreement with the theoretical dashed lines. A small decrease in the size of the electron pockets is observed. For the reconstructed bands, as explained, the statistics are not as good, but we can still see a decreasing trend in the data, which closely follows the dashed theoretical lines. The exception is the result obtained for a cut along the YZ direction in the case of the Cr8.5% sample. Nonetheless, we can confirm that the electron pockets are slightly decreasing, a tendency relatively well described by our theoretical predictions.

In addition to our detailed analysis of the states close to the FS, we now turn attention to electronic states with large E_B, to evaluate the validity and limitations of our theoretical approximations. In Fig. 4(a), we compare the bands with d_{z^2} main orbital character [60], at $E_b \approx -0.45$ eV, for the BFA and Cr8.5% samples. The orange arrows show the maximum spectral weight position at the $k_z = 0$ cut. This band position is shifted up, which was also observed for MnBFA as shown in Fig. 4(b), where we also compare with our theoretical scenarios (dashed lines). The VCA approximation predicts a larger shift than the observed one. Thus, the experimental trend is better described by considering only the structural effects on atomic distances, suggesting that the shift in the d_z^2 derived band can be associated with the change in the orbital hybridizations caused by the chemical substitution. Indeed, this effect is more prominent in MnBFA, where charge doping is barely observed [30]. A more qualitative observation is that the bottom of the bands forming the electron pockets is weakly dependent on Cr content, further illustrating that states with larger E_B are less affected by the charge doping and better described without the VCA.

Based on the overall agreement between experiments and our VCA calculations, we can assert that the role of Cr as a hole dopant in CrBFA is transparent for states in the vicinity of the FS and is in sharp contrast to the case of Mn-substituted samples [26, 27, 30, 34]. Nevertheless, the structural changes affecting the orbital hybridization are important to describe the entirety of the electronic structure, affecting mainly the states at larger E_B.

We now turn to an analysis of the ARPES spectral function to extract the scattering rate $\Gamma(E_B)$ and the one-particle self-energy imaginary part $\text{Im}\Sigma(E_B)$ to characterize electronic correlations in the system. We fit momentum distribution curves (MDCs) to the expression for the one-particle spectral function $A(\boldsymbol{k}, E_B)$ for a system of weakly correlated electrons [61]. The focus is to extract $\Gamma(E_B)$ and $\text{Im}\Sigma(E_B)$ from the MDCs analysis for the band with d_{yz} main orbital character in the measurements in direction ΓX with LV polarization, represented as green hole pockets of Fig. 1($a - c$).

In Fig. 4(c)-(d) we present these fittings for the BFA and Cr8.5% samples, obtained as
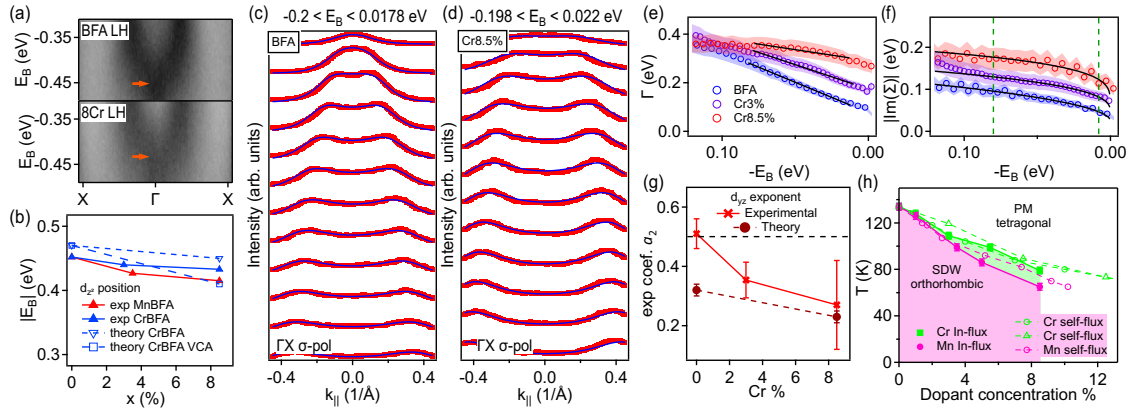
Figure 4: (a) Comparison of higher E_B band (d_{z^2} character) at Γ point for BFA and Cr8.5% samples. (b) This band position as a function of dopant concentration for the MnBFA and theoretical values for CrBFA. (c)-(d) ARPES spectral function analysis for the two samples showing fittings (blue lines) of several MDCs (red dots) for increasing binding energies. The extracted quantities (e) $\Gamma(E_B)$ and (f) $\text{Im}\Sigma(E_B)$ for the d_{yz}-derived hole pocket, the shaded area represent the error bars. The solid black lines represent fittings close to E_F that are linear for $\Gamma(E_B)$ and a power-law for $\text{Im}\Sigma(E_B)$. (g) The fitted exponents of (f) as a function of Cr content compared with the calculated ones. The values are those in Table 1. (h) T vs. x phase diagram comparing CrBFA samples used in this study with MnBFA samples grown by the In-flux method. The results for the self-flux grown samples are from references [23, 24, 35]. Care was taken to compare T_{SDW} values obtained by the same method.

Table 1: Self-energy imaginary part $\mathrm{Im}\Sigma(E_B)$ fitting coefficients obtained from the theoretical calculations and experimental data for the bands derived from the d_{yz} orbital. The fitted function is $|\mathrm{Im}\Sigma(E_B)| = a_0 + a_1(-E_B)^{a_2}$.

Orbital	Fitting	BFA			Cr8.5%		
		a_0	a_1	a_2	a_0	a_1	a_2
d_{z^2}	theory	-0.19(4)	0.82(4)	0.42(3)	-0.27(6)	0.97(6)	0.35(3)
$d_{x^2-y^2}$	theory	-0.15(3)	0.74(3)	0.44(2)	-0.21(4)	0.85(4)	0.38(2)
d_{xz}	theory	-0.29(4)	0.95(4)	0.32(2)	-0.52(6)	1.26(6)	0.22(1)
d_{yz}	theory	-0.27(4)	0.93(4)	0.32(2)	-0.47(7)	1.21(7)	0.23(2)
	exp.	0.02(1)	0.26(6)	0.50(5)	0.05(2)	0.23(6)	0.27(15)
d_{xy}	theory	-0.41(7)	1.08(7)	0.26(2)	-1.34(31)	2.11(32)	0.12(2)

in Refs. [62, 63]. A clear necessary caution with this type of analysis is that substitutional disorder contributes with extrinsic effects to the broadening of the spectroscopic features. In turn, it poses a challenge to the determination of $\Gamma(E_B)$ and thus of $\mathrm{Im}\Sigma(E_B)$. To evade this problem, we focus on these quantities scaling, which already contain all qualitative information about the correlated nature of the electronic states in our samples, and are robust against the homogeneous broadening due to disorder. With this in mind, we can analyze the extracted values of $\Gamma(E_B)$ and the calculated $\mathrm{Im}\Sigma(E_B)$ as a function of E_B, shown in Figs. 4(e) and (f) for all samples. The shaded area represents the error bars.

It is clear that $\Gamma(E_B)$ and $\mathrm{Im}\Sigma(E_B)$ are not proportional to each other and do not follow a quadratic behavior, which would be expected for a normal Fermi liquid. This is an indication of the correlated nature of the metallic state in BFA and CrBFA and was also observed for other substitutions [30, 62, 63, 64]. In the case of the scattering rates, this is qualitatively captured by the lines drawn in Fig. 4(e), which suggest that $\Gamma(E_B)$ can be described as a linear function of E_B close to E_F.

It is tempting to assert that Cr causes the decrease of the quasiparticle lifetime at E_F. We caution, however, that this effect may not be an intrinsic electronic effect, but rather the extrinsic effect introduced by chemical substitution. Focusing on the rate of change of $\Gamma(E_B)$ close to E_F (the line slops), it seems that the scattering rates are only weakly dependent on Cr content. In the case of MnBFA, a stronger dependence was found [30].

Most interesting, the $\mathrm{Im}\Sigma(E_B)$ for all samples present a fractional scaling close to $\sqrt{-E_B}$, the hallmark of a Hund's metal [46, 65]. The data is presented in Fig. 4(f) and the fractional behavior is shown as a fitting to the function $|\mathrm{Im}\Sigma(E_B)| = a_0 + a_1(-E_B)^{a_2}$, represented by the black solid lines. Only points between the two green dashed lines were considered for the fitting, excluding the points close to the E_F within the binding energy resolution and points too far from the FS.

A similar fitting was performed for the DFT+DMFT obtained self-energies on the Matsubara axis (imaginary axis) for the BFA and Cr8.5% samples. Results of the analysis for the theoretical data are presented in Table 1 for all bands, along with the experimental result for the band with main d_{yz} orbital character.

The a_0 and a_1 coefficients determined from experiments do not follow a particular trend, which can be expected since they are closely related to the disorder and the self-energy extraction method. The power-law scaling, however, which is related to the a_2 coefficient, has a robust trend. For comparison, theoretical and experimental results are compiled in Fig. 4(g). The experiments and theory compare well, with a_2 tending to decrease as a function of Cr concentration. The dashed black line is drawn to pinpoint the value of 0.5 corresponding to a square root dependency of $\mathrm{Im}\Sigma(E_B)$ with E_B.

In Fig. 4(h) we show the phase diagrams for the CrBFA samples used in this work and

compare them with other CrBFA and MnBFA samples. We emphasize that the present phase diagram for In-flux grown samples is in agreement with those of self-flux grown samples [23, 24, 35]. By inspecting the phase diagrams, one can either conclude that the suppression of T_{SDW} follows nearly the same pace as a function of x for Cr and Mn samples. It is possible that this conclusion only holds for really small x, but that for larger x (around $x > 0.04$), Mn is more efficient than Cr in suppressing T_{SDW}. In any case, it seems fair to conclude that the evolution of T_{SDW} in the cases of MnBFA and CrBFA is not strongly dependent on the nature of the substituent atom, despite the rather distinct effects of Cr and Mn on the low energy degrees of freedom, with Cr acting as an efficient hole dopant, while Mn does not. Thus, the electronic bands tuning near E_F, by either Cr or Mn, is not controlling T_{SDW}. Rather, we suggest that the scattering between the competing SDW and Néel phases derived, respectively, from the Fe and Cr/Mn spins is the main control parameter. This mechanism only depends on the total amount of extrinsic spins introduced in the Fe lattice, and therefore only depends on x. Some extra scattering in the case of Mn may originate from the glassy magnetic behavior introduced by Mn [43] and from the fact that Mn^{2+} introduces $S = 5/2$ spins whereas Cr^{2+} introduces $S = 2$ spins, and the latter is the same spin type of the Fe^{2+} lattice.

4   Conclusion

The most transparent result of our paper is that the partial substitution of Fe by Cr causes an effective hole doping of the electronic states in the vicinity of the FS. This is supported by the agreement between our experiments and calculations, with the doping effects emulated by VCA being the relevant approximation closer to E_F. We then proceed to discuss results based on our analysis of the ARPES spectral functions. We found that the imaginary part of the self-energy, $\text{Im}\Sigma(E_B)$, presents a Cr-dependent fractional scaling as a function of the binding energy, a common feature of Hund's metals. This scaling behavior was also observed in our DFT+DMFT calculations.

By comparing x vs. T phase diagrams for CrBFA and MnBFA, we concluded that the suppression of T_{SDW} cannot depend on the effects caused by Cr and Mn on the Fermi surfaces. It is thus suggested that low-energy effective models are not adequate to understand the evolution of magnetism for these substitutions.

The characterization of CrBFA and MnBFA as a Hund's metal naturally explains these results. A recent analysis of Mn and Cr substituted 1144 FeSCs materials [66, 67], also suggests that the amount of doped holes is not controlling the suppression of T_C and T_{SDW} for Cr and Mn substitutions, making the breakdown of the low-energy effective models possibly more ubiquitous.

Recently, it was suggested that the Cr doping of $CsFe_2As_2$ could push the orbital-selective Hund's metal system further into a strongly correlated electronic phase reminiscent of Heavy Fermion quantum criticality [68]. This agrees with our findings in the low Cr-doping region, where we could observe the increasing electronic correlations induced by Cr.

Finally, based on the totality of our analysis, we conclude that SC is lacking in CrBFA mainly because of the competition between the Cr local moments and the Fe magnetism. Indeed, what distinguishes CrBFA and K-substituted samples are the distinct magnetic fluctuations that compete for the magnetic ground state in CrBFA.

Acknowledgements

We thank Claude Monney for fruitful discussions. We acknowledge the MAX IV Laboratory for beamtime on the Bloch Beamline under Proposal 20200293 and the support of Gerardina Carbone and Craig Polley during experiments.

Author contributions F.A.G. designed the project. K.R., G.S.F., P.G.P., and C.A. were responsible for the single crystal growth and characterization. M.R.C., B.S., P.H.A.M., and F.A.G. performed the ARPES experiments. M.R.C. conducted the ARPES data processing and analysis. W.H.B. performed the DFT calculations. The draft was written by M.R.C., W.H.B. and F.A.G. with inputs from all co-authors.

Funding information The Fundação de Amparo à Pesquisa do Estado de São Paulo financial support is acknowledged by M.R.C. (Grants No. 2019/05150-7 and No. 2020/13701-0), F.A.G. (Grant No. 2019/25665-1); K.R.P., P.G.P. and C.A. (Grant No. 2017/10581-1). B.S. acknowledges funding from the Swiss National Science Foundation (SNSF) Grant No. P00P2_170597. P.G.P. and C.A. acknowledge financial support from CNPq: Grants No. 304496/2017-0, 310373/2019-0, and 311783/2021-0. W.H.B acknowledges the financial support from CNPq Grant No. 402919/2021-1, FAPEMIG, and the computational centers: National Laboratory for Scientific Computing (LNCC/MCTI, Brazil), for providing HPC resources of the SDumont supercomputer (http://sdumont.lncc.br), and CENAPAD-SP.

References

[1] Y. Kamihara, T. Watanabe, M. Hirano and H. Hosono, *Iron-Based Layered Superconductor La[O1-xFx]FeAs (x = 0.05-0.12) with Tc = 26 K*, J. Am. Chem. Soc. **130**(11), 3296 (2008), doi:10.1021/ja800073m.

[2] R. Zhi-An, L. Wei, Y. Jie, Y. Wei, S. Xiao-Li, Zheng-Cai, C. Guang-Can, D. Xiao-Li, S. Li-Ling, Z. Fang and Z. Zhong-Xian, *Superconductivity at 55 K in Iron-Based F-Doped Layered Quaternary Compound Sm[O1-xFx] FeAs*, Chinese Physics Letters **25**(6), 2215 (2008), doi:10.1088/0256-307X/25/6/080.

[3] H. Hosono and K. Kuroki, *Iron-based superconductors: Current status of materials and pairing mechanism*, Physica C: Superconductivity and its Applications **514**, 399 (2015), doi:https://doi.org/10.1016/j.physc.2015.02.020, Superconducting Materials: Conventional, Unconventional and Undetermined.

[4] M. Rotter, M. Tegel, D. Johrendt, I. Schellenberg, W. Hermes and R. Pöttgen, *Spin-density-wave anomaly at 140 k in the ternary iron arsenide $bafe_2as_2$*, Phys. Rev. B **78**, 020503(R) (2008), doi:10.1103/PhysRevB.78.020503.

[5] M. G. Kim, R. M. Fernandes, A. Kreyssig, J. W. Kim, A. Thaler, S. L. Bud'ko, P. C. Canfield, R. J. McQueeney, J. Schmalian and A. I. Goldman, *Character of the structural and magnetic phase transitions in the parent and electron-doped $BaFe_2As_2$ compounds*, Physical Review B **83**(13), 134522 (2011), doi:10.1103/PhysRevB.83.134522.

[6] N. Ni, A. Thaler, A. Kracher, J. Q. Yan, S. L. Bud'ko and P. C. Canfield, *Phase diagrams of $Ba(Fe_{1-x}M_x)_2As_2$ single crystals (M = Rh and Pd)*, Physical Review B **80**(2), 024511 (2009), doi:10.1103/PhysRevB.80.024511.

[7] A. S. Sefat, R. Jin, M. A. McGuire, B. C. Sales, D. J. Singh and D. Mandrus, *Superconductivity at 22 K in co-doped $BaFe_2As_2$ crystals*, Phys. Rev. Lett. **101**, 117004 (2008), doi:10.1103/PhysRevLett.101.117004.

[8] L. J. Li, Y. K. Luo, Q. B. Wang, H. Chen, Z. Ren, Q. Tao, Y. K. Li, X. Lin, M. He, Z. W. Zhu, G. H. Cao and Z. A. Xu, *Superconductivity induced by Ni doping in $BaFe_2As_2$ singlecrystals*, New Journal of Physics **11**(2), 025008 (2009), doi:10.1088/1367-2630/11/2/025008.

[9] J.-H. Chu, J. G. Analytis, C. Kucharczyk and I. R. Fisher, *Determination of the phase diagram of the electron-doped superconductor $Ba(Fe_{1-x}Co_x)_2As_2$*, Phys. Rev. B **79**, 014506 (2009), doi:10.1103/PhysRevB.79.014506.

[10] S. Jiang, H. Xing, G. Xuan, C. Wang, Z. Ren, C. Feng, J. Dai, Z. Xu and G. Cao, *Superconductivity up to 30 k in the vicinity of the quantum critical point in $BaFe_2(As_{1-x}P_x)_2$*, Journal of Physics: Condensed Matter **21**(38), 382203 (2009), doi:10.1088/0953-8984/21/38/382203.

[11] S. R. Saha, T. Drye, K. Kirshenbaum, N. P. Butch, P. Y. Zavalij and J. Paglione, *Superconductivity at 23 K in Pt doped BaFe2As2 single crystals*, Journal of Physics: Condensed Matter **22**(7), 072204 (2010), doi:10.1088/0953-8984/22/7/072204.

[12] M. Rotter, M. Tegel and D. Johrendt, *Superconductivity at 38 K in the iron arsenide $(Ba_{1-x}K_x)Fe_2As_2$*, Phys. Rev. Lett. **101**, 107006 (2008), doi:10.1103/PhysRevLett.101.107006.

[13] K. Sasmal, B. Lv, B. Lorenz, A. M. Guloy, F. Chen, Y.-Y. Xue and C.-W. Chu, *Superconducting fe-based compounds $(A_{1-x}Sr_x)Fe_2As_2$ with A = K and cs with transition temperatures up to 37 K*, Phys. Rev. Lett. **101**, 107007 (2008), doi:10.1103/PhysRevLett.101.107007.

[14] R. M. Fernandes, A. I. Coldea, H. Ding, I. R. Fisher, P. J. Hirschfeld and G. Kotliar, *Iron pnictides and chalcogenides: a new paradigm for superconductivity*, Nature **601**(7891), 35 (2022), doi:10.1038/s41586-021-04073-2.

[15] R. M. Fernandes and A. V. Chubukov, *Low-energy microscopic models for iron-based superconductors: a review*, Rep. Prog. Phys. **80**(1), 014503 (2016), doi:10.1088/1361-6633/80/1/014503.

[16] A. Chubukov, *Pairing Mechanism in Fe-Based Superconductors*, Annual Review of Condensed Matter Physics **3**(1), 57 (2012), doi:10.1146/annurev-conmatphys-020911-125055.

[17] K. Haule and G. Kotliar, *Coherence–incoherence crossover in the normal state of iron oxypnictides and importance of Hund's rule coupling*, New Journal of Physics **11**(2), 025021 (2009), doi:10.1088/1367-2630/11/2/025021.

[18] Z. P. Yin, K. Haule and G. Kotliar, *Kinetic frustration and the nature of the magnetic and paramagnetic states in iron pnictides and iron chalcogenides*, Nature Materials **10**(12), 932 (2011), doi:10.1038/NMAT3120.

[19] Z. P. Yin, K. Haule and G. Kotliar, *Magnetism and charge dynamics in iron pnictides*, Nature Physics **7**(4), 294 (2011), doi:10.1038/NPHYS1923.

[20] E. Bascones, B. Valenzuela and M. Jose Calderon, *Magnetic interactions in iron superconductors: A review*, Comptes Rendus Physique **17**(1-2), 36 (2016), doi:10.1016/j.crhy.2015.05.004.

[21] R. M. Fernandes, A. I. Coldea, H. Ding, I. R. Fisher, P. J. Hirschfeld and G. Kotliar, *Iron pnictides and chalcogenides: a new paradigm for superconductivity*, Nature **601**(7891), 35 (2022), doi:10.1038/s41586-021-04073-2.

[22] T.-H. Lee, A. Chubukov, H. Miao and G. Kotliar, *Pairing Mechanism in Hund's Metal Superconductors and the Universality of the Superconducting Gap to Critical Temperature Ratio*, Physical Review Letters **121**(18), 187003 (2018), doi:10.1103/PhysRevLett.121.187003.

[23] A. S. Sefat, D. J. Singh, L. H. VanBebber, Y. Mozharivskyj, M. A. McGuire, R. Jin, B. C. Sales, V. Keppens and D. Mandrus, *Absence of superconductivity in hole-doped $BaFe_{2-x}Cr_xAs_2$ single crystals*, Phys. Rev. B **79**, 224524 (2009), doi:10.1103/PhysRevB.79.224524.

[24] A. Thaler, H. Hodovanets, M. S. Torikachvili, S. Ran, A. Kracher, W. Straszheim, J. Q. Yan, E. Mun and P. C. Canfield, *Physical and magnetic properties of $Ba(Fe_{1-x}Mn_x)_2As_2$ single crystals*, Physical Review B **84**(14), 144528 (2011), doi:10.1103/PhysRevB.84.144528.

[25] X.-G. Li, J.-M. Sheng, C.-K. Tian, Y.-Y. Wang, T.-L. Xia, L. Wang, F. Ye, W. Tian, J.-C. Wang, J.-J. Liu, H.-X. Zhang, W. Bao *et al.*, *Effects of vanadium doping on BaFe2As2*, Europhysics Letters **122**(6), 67006 (2018), doi:10.1209/0295-5075/122/67006.

[26] Y. Texier, Y. Laplace, P. Mendels, J. T. Park, G. Friemel, D. L. Sun, D. S. Inosov, C. T. Lin and J. Bobroff, *Mn local moments prevent superconductivity in iron pnictides $Ba(Fe_{1-x}Mn_x)_2As_2$*, EPL (Europhysics Letters) **99**(1), 17002 (2012), doi:10.1209/0295-5075/99/17002.

[27] H. Suzuki, T. Yoshida, S. Ideta, G. Shibata, K. Ishigami, T. Kadono, A. Fujimori, M. Hashimoto, D. H. Lu, Z.-X. Shen, K. Ono, E. Sakai *et al.*, *Absence of superconductivity in the hole-doped Fe pnictide $Ba(Fe_{1-x}Mn_x)_2As_2$: Photoemission and x-ray absorption spectroscopy studies*, Physical Review B **88**(10), 100501(R) (2013), doi:10.1103/PhysRevB.88.100501.

[28] G. S. Tucker, D. K. Pratt, M. G. Kim, S. Ran, A. Thaler, G. E. Granroth, K. Marty, W. Tian, J. L. Zarestky, M. D. Lumsden, S. L. Bud'ko, P. C. Canfield *et al.*, *Competition between stripe and checkerboard magnetic instabilities in Mn-doped $BaFe_2As_2$*, Physical Review B **86**(2), 020503(R) (2012), doi:10.1103/PhysRevB.86.020503.

[29] F. A. Garcia, O. Ivashko, D. E. McNally, L. Das, M. M. Piva, C. Adriano, P. G. Pagliuso, J. Chang, T. Schmitt and C. Monney, *Anisotropic magnetic excitations and incipient Néel order in $Ba(Fe_{1-x}Mn_x)_2As_2$*, Phys. Rev. B **99**, 115118 (2019), doi:10.1103/PhysRevB.99.115118.

[30] M. R. Cantarino, K. R. Pakuszewski, B. Salzmann, P. H. A. Moya, W. R. d. S. Neto, G. S. Freitas, P. G. Pagliuso, W. H. Brito, C. Monney, C. Adriano and F. A. Garcia, *Incoherent electronic band states in Mn-substituted $BaFe_2As_2$*, Phys. Rev. B **108**, 245124 (2023), doi:10.1103/PhysRevB.108.245124.

[31] R. M. Fernandes and A. J. Millis, *Suppression of Superconductivity by Néel-Type Magnetic Fluctuations in the Iron Pnictides*, Physical Review Letters **110**(11), 117004 (2013), doi:10.1103/PhysRevLett.110.117004.

[32] M. N. Gastiasoro and B. M. Andersen, *Enhancement of Magnetic Stripe Order in Iron-Pnictide Superconductors from the Interaction between Conduction Electrons and Magnetic Impurities*, Physical Review Letters **113**(6), 067002 (2014), doi:10.1103/PhysRevLett.113.067002.

[33] M. N. Gastiasoro, F. Bernardini and B. M. Andersen, *Unconventional Disorder Effects in Correlated Superconductors*, Physical Review Letters **117**(25), 257002 (2016), doi:10.1103/PhysRevLett.117.257002.

[34] T. Kobayashi, M. Nakajima, S. Miyasaka and S. Tajima, *Carrier localization due to local magnetic order induced by magnetic impurities in $Ba(Fe_{1-x}TM_x)_2As_2$ ($TM = Mn$ and Cr) as seen via optical spectra*, Physical Review B **94**(22), 224516 (2016), doi:10.1103/PhysRevB.94.224516.

[35] J. P. Clancy, B. D. Gaulin and A. S. Sefat, *High-resolution x-ray scattering studies of structural phase transitions in $Ba(Fe_{1-x}Cr_x)_2As_2$*, Physical Review B **85**(5), 054115 (2012), doi:10.1103/PhysRevB.85.054115.

[36] K. Marty, A. D. Christianson, C. H. Wang, M. Matsuda, H. Cao, L. H. VanBebber, J. L. Zarestky, D. J. Singh, A. S. Sefat and M. D. Lumsden, *Competing magnetic ground states in nonsuperconducting $Ba(Fe_{1-x}Cr_x)_2As_2$ as seen via neutron diffraction*, Phys. Rev. B **83**, 060509(R) (2011), doi:10.1103/PhysRevB.83.060509.

[37] K. A. Filsinger, W. Schnelle, P. Adler, G. H. Fecher, M. Reehuis, A. Hoser, J.-U. Hoffmann, P. Werner, M. Greenblatt and C. Felser, *Antiferromagnetic structure and electronic properties of BaCr2As2 and BaCrFeAs2*, Physical Review B **95**(18), 184414 (2017), doi:10.1103/PhysRevB.95.184414.

[38] Q. Zou, M. Fu, Z. Wu, L. Li, D. S. Parker, A. S. Sefat and Z. Gai, *Competitive and cooperative electronic states in $Ba(Fe_{1-x}T_x)_2As_2$ with $T = Co$, Ni, Cr*, npj Quantum Materials **6**(1), 1 (2021), doi:10.1038/s41535-021-00385-8.

[39] D. Gong, T. Xie, R. Zhang, J. Birk, C. Niedermayer, F. Han, S. H. Lapidus, P. Dai, S. Li and H. Luo, *Doping effects of cr on the physical properties of $BaFe_{1.9-x}Ni_{0.1}Cr_xAs_2$*, Phys. Rev. B **98**, 014512 (2018), doi:10.1103/PhysRevB.98.014512.

[40] R. Zhang, D. Gong, X. Lu, S. Li, M. Laver, C. Niedermayer, S. Danilkin, G. Deng, P. Dai and H. Luo, *Doping evolution of antiferromagnetism and transport properties in nonsuperconducting $BaFe_{2-2x}Ni_xCr_xAs_2$*, Phys. Rev. B **91**, 094506 (2015), doi:10.1103/PhysRevB.91.094506.

[41] D. Gong, M. Yi, M. Wang, T. Xie, W. Zhang, S. Danilkin, G. Deng, X. Liu, J. T. Park, K. Ikeuchi, K. Kamazawa, S.-K. Mo *et al.*, *Nematic fluctuations in the nonsuperconducting iron pnictide $BaFe_{1.9-x}Ni_{0.1}Cr_xAs_2$*, Frontiers in Physics **10** (2022), doi:10.3389/fphy.2022.886459.

[42] W. Zhang, Y. Wei, T. Xie, Z. Liu, D. Gong, X. Ma, D. Hu, P. Čermák, A. Schneidewind, G. Tucker, S. Meng, Z. Huesges *et al.*, *Unconventional antiferromagnetic quantum critical point in $Ba(Fe_{0.97}Cr_{0.03})_2(As_{1-x}P_x)_2$*, Phys. Rev. Lett. **122**, 037001 (2019), doi:10.1103/PhysRevLett.122.037001.

[43] D. S. Inosov, G. Friemel, J. T. Park, A. C. Walters, Y. Texier, Y. Laplace, J. Bobroff, V. Hinkov, D. L. Sun, Y. Liu, R. Khasanov, K. Sedlak *et al.*, *Possible realization of an antiferromagnetic griffiths phase in Ba(Fe$_{1-x}$Mn$_x$)$_2$As$_2$*, Phys. Rev. B **87**, 224425 (2013), doi:10.1103/PhysRevB.87.224425.

[44] S. J. Li, D. Zhao, S. Wang, S. T. Cui, N. Z. Wang, J. Li, D. W. Song, B. L. Kang, L. X. Zheng, L. P. Nie, Z. M. Wu, Y. B. Zhou *et al.*, *Emergent spin-glass state in the doped hund's metal CsFe$_2$As$_2$*, Phys. Rev. B **107**, 115144 (2023), doi:10.1103/PhysRevB.107.115144.

[45] C. Liu, G. D. Samolyuk, Y. Lee, N. Ni, T. Kondo, A. F. Santander-Syro, S. L. Bud'ko, J. L. McChesney, E. Rotenberg, T. Valla, A. V. Fedorov, P. C. Canfield *et al.*, *K-doping dependence of the fermi surface of the iron-arsenic Ba$_{1-x}$K$_x$Fe$_2$As$_2$ superconductor using angle-resolved photoemission spectroscopy*, Phys. Rev. Lett. **101**, 177005 (2008), doi:10.1103/PhysRevLett.101.177005.

[46] K. M. Stadler, G. Kotliar, S.-S. B. Lee, A. Weichselbaum and J. von Delft, *Differentiating Hund from Mott physics in a three-band Hubbard-Hund model: Temperature dependence of spectral, transport, and thermodynamic properties*, Physical Review B **104**(11), 115107 (2021), doi:10.1103/PhysRevB.104.115107.

[47] P. Werner, E. Gull, M. Troyer and A. J. Millis, *Spin freezing transition and non-fermi-liquid self-energy in a three-orbital model*, Phys. Rev. Lett. **101**, 166405 (2008), doi:10.1103/PhysRevLett.101.166405.

[48] T. M. Garitezi, C. Adriano, P. F. S. Rosa, E. M. Bittar, L. Bufaiçal, R. L. d. Almeida, E. Granado, T. Grant, Z. Fisk, M. A. Avila, R. A. Ribeiro, P. L. Kuhns *et al.*, *Synthesis and Characterization of BaFe2As2 Single Crystals Grown by In-flux Technique*, Brazilian Journal of Physics **43**(4), 223 (2013), doi:10.1007/s13538-013-0144-z.

[49] K. Haule, C.-H. Yee and K. Kim, *Dynamical mean-field theory within the full-potential methods: Electronic structure of CeIrIn$_5$, CeCoIn$_5$, and CeRhIn$_5$*, Phys. Rev. B **81**, 195107 (2010), doi:10.1103/PhysRevB.81.195107.

[50] J. P. Perdew, K. Burke and M. Ernzerhof, *Generalized gradient approximation made simple*, Phys. Rev. Lett. **77**, 3865 (1996), doi:10.1103/PhysRevLett.77.3865.

[51] P. Blaha, G. K. H. Madsen, D. Kvasnicka and J. Luitz, *WIEN2K, An Augmented Plane Wave + Local Orbitals Program for Calculating Crystal Properties*, Karlheinz Schwarz, Techn. Universität Wien, Austria (2001).

[52] K. Haule, *Quantum monte carlo impurity solver for cluster dynamical mean-field theory and electronic structure calculations with adjustable cluster base*, Phys. Rev. B **75**, 155113 (2007), doi:10.1103/PhysRevB.75.155113.

[53] V. I. Anisimov, F. Aryasetiawan and A. I. Lichtenstein, *First-principles calculations of the electronic structure and spectra of strongly correlated systems: the lda+ u method*, Journal of Physics: Condensed Matter **9**(4), 767 (1997), doi:10.1088/0953-8984/9/4/002.

[54] M. Fuglsang Jensen, V. Brouet, E. Papalazarou, A. Nicolaou, A. Taleb-Ibrahimi, P. Le Fèvre, F. Bertran, A. Forget and D. Colson, *Angle-resolved photoemission study of the role of nesting and orbital orderings in the antiferromagnetic phase of BaFe$_2$As$_2$*, Physical Review B **84**(1), 014509 (2011), doi:10.1103/PhysRevB.84.014509.

[55] V. Brouet, M. F. Jensen, P.-H. Lin, A. Taleb-Ibrahimi, P. Le Fèvre, F. Bertran, C.-H. Lin, W. Ku, A. Forget and D. Colson, *Impact of the two Fe unit cell on the electronic structure measured by ARPES in iron pnictides*, Physical Review B **86**(7), 075123 (2012), doi:10.1103/PhysRevB.86.075123.

[56] M. Yi, Y. Zhang, Z.-X. Shen and D. Lu, *Role of the orbital degree of freedom in iron-based superconductors*, npj Quantum Materials **2**(1), 57 (2017), doi:10.1038/s41535-017-0059-y.

[57] H. Pfau, C. R. Rotundu, J. C. Palmstrom, S. D. Chen, M. Hashimoto, D. Lu, A. F. Kemper, I. R. Fisher and Z.-X. Shen, *Detailed band structure of twinned and detwinned $BaFe_2As_2$ studied with angle-resolved photoemission spectroscopy*, Phys. Rev. B **99**, 035118 (2019), doi:10.1103/PhysRevB.99.035118.

[58] Y. Zhang, F. Chen, C. He, B. Zhou, B. P. Xie, C. Fang, W. F. Tsai, X. H. Chen, H. Hayashi, J. Jiang, H. Iwasawa, K. Shimada *et al.*, *Orbital characters of bands in the iron-based superconductor $BaFe_{1.85}Co_{0.15}As_2$*, Phys. Rev. B **83**(5), 054510 (2011), doi:10.1103/PhysRevB.83.054510.

[59] A. G. de Figueiredo, M. R. Cantarino, W. R. da Silva Neto, K. R. Pakuszewski, R. Grossi, D. S. Christovam, J. C. Souza, M. M. Piva, G. S. Freitas, P. G. Pagliuso, C. Adriano and F. A. Garcia, *Orbital localization and the role of the fe and as 4p orbitals in $BaFe_2As_2$ probed by xanes*, Phys. Rev. B **105**, 045130 (2022), doi:10.1103/PhysRevB.105.045130.

[60] S. Graser, A. F. Kemper, T. A. Maier, H.-P. Cheng, P. J. Hirschfeld and D. J. Scalapino, *Spin fluctuations and superconductivity in a three-dimensional tight-binding model for $BaFe_2As_2$*, Phys. Rev. B **81**, 214503 (2010), doi:10.1103/PhysRevB.81.214503.

[61] J. A. Sobota, Y. He and Z.-X. Shen, *Angle-resolved photoemission studies of quantum materials*, Reviews of Modern Physics **93**(2), 025006 (2021), doi:10.1103/RevModPhys.93.025006.

[62] R. Kurleto and J. Fink, *About two-dimensional fits for the analysis of the scattering rates and renormalization functions from angle-resolved photoelectron spectroscopy data*, Journal of Electron Spectroscopy and Related Phenomena **253**, 147127 (2021), doi:10.1016/j.elspec.2021.147127.

[63] J. Fink, E. D. L. Rienks, M. Yao, R. Kurleto, J. Bannies, S. Aswartham, I. Morozov, S. Wurmehl, T. Wolf, F. Hardy, C. Meingast, H. S. Jeevan *et al.*, *Linkage between scattering rates and superconductivity in doped ferropnictides*, Physical Review B **103**(15), 155119 (2021), doi:10.1103/PhysRevB.103.155119.

[64] J. Fink, E. D. L. Rienks, S. Thirupathaiah, J. Nayak, A. van Roekeghem, S. Biermann, T. Wolf, P. Adelmann, H. S. Jeevan, P. Gegenwart, S. Wurmehl, C. Felser *et al.*, *Experimental evidence for importance of Hund's exchange interaction for incoherence of charge carriers in iron-based superconductors*, Phys. Rev. B **95**, 144513 (2017), doi:10.1103/PhysRevB.95.144513.

[65] Z. P. Yin, K. Haule and G. Kotliar, *Fractional power-law behavior and its origin in iron-chalcogenide and ruthenate superconductors: Insights from first-principles calculations*, Physical Review B **86**(19), 195141 (2012), doi:10.1103/PhysRevB.86.195141.

[66] M. Xu, J. Schmidt, E. Gati, L. Xiang, W. R. Meier, V. G. Kogan, S. L. Bud'ko and P. C. Canfield, *Superconductivity and phase diagrams of $CaK(Fe_{1-x}Mn_x)_4As_4$ single crystals*, Phys. Rev. B **105**, 214526 (2022), doi:10.1103/PhysRevB.105.214526.

[67] M. Xu, J. Schmidt, M. A. Tanatar, R. Prozorov, S. L. Bud'ko and P. C. Canfield, *Superconductivity and magnetic and transport properties of single-crystalline $CaK(Fe_{1-x}Cr_x)_4As_4$*, Phys. Rev. B **107**, 134511 (2023), doi:10.1103/PhysRevB.107.134511.

[68] M. Crispino, P. V. Arribi, A. Shukla, F. Hardy, A.-A. Haghighirad, T. Wolf, R. Heid, C. Meingast, T. Gorni, A. Avella and L. d. Medici, *Paradigm for finding d-electron heavy fermions: the case of Cr-doped $CsFe_2As_2$*, arXiv (arXiv:2312.06511) (2023), doi:10.48550/arXiv.2312.06511, `2312.06511[cond-mat]`.